Article

Cell Systems

Optogenetic control of the integrated stress response reveals proportional encoding and the stress memory landscape

Graphical abstract

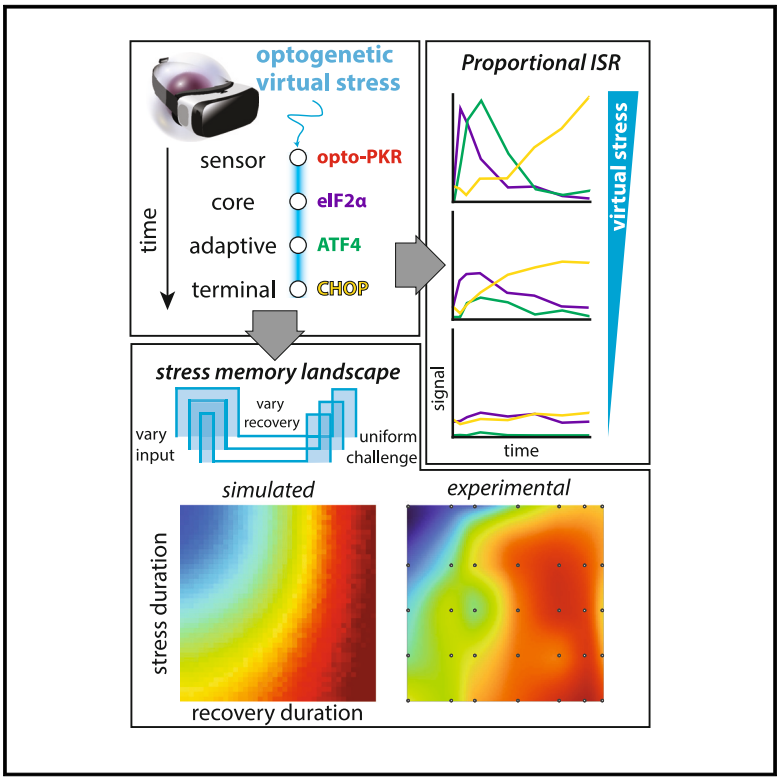

Authors

Taivan Batjargal, Francesca Zappa, Ryan J. Grant, ..., Siddharth S. Dey, Diego Acosta-Alvear, Maxwell Z. Wilson

Correspondence

daa@lifesci.ucsb.edu (D.A.-A.), mzw@ucsb.edu (M.Z.W.)

In brief

Batjargal et al. developed a novel optogenetic tool to virtually stress cells, allowing them to tune the input dynamics with light. They (1) reveal that ISR pathway responds in proportion to varying virtual stress levels and (2) map the relationship between past stresses to future responses through experimental and computational methods.

Highlights

- Optogenetic activation of PKR induces a stressless stress response
- The ISR has early and late phases corresponding to adaptive and terminal outcomes
- Key ISR pathway nodes respond proportionally to the intensity of the stress input
- Both the model and experiment map the dependence of future responses on past ISR activations

Batjargal et al., 2023, Cell Systems *14*, 551–562
July 19, 2023
https://doi.org/10.1016/j.cels.2023.06.001

CellPress

Cell Systems

CellPress

Article

Optogenetic control of the integrated stress response reveals proportional encoding and the stress memory landscape

Taivan Batjargal,[2] Francesca Zappa,[3,6] Ryan J. Grant,[3] Robert A. Piscopio,[3] Alex Chialastri,[5] Siddharth S. Dey,[1,4,5] Diego Acosta-Alvear,[2,3,4,6,*] and Maxwell Z. Wilson[1,2,3,4,7,*]

[1]Center for BioEngineering, University of California Santa Barbara, Santa Barbara, CA, USA
[2]Biomolecular Science and Engineering Program, University of California Santa Barbara, Santa Barbara, CA, USA
[3]Department of Molecular, Cellular, and Developmental Biology, University of California Santa Barbara, Santa Barbara, CA, USA
[4]Neuroscience Research Institute, University of California Santa Barbara, Santa Barbara, CA, USA
[5]Department of Chemical Engineering, University of California Santa Barbara, Santa Barbara, CA, USA
[6]Present address: Altos Labs Bay Area Institute of Science, Altos Labs, Inc., San Francisco, CA, USA
[7]Lead contact
*Correspondence: daa@lifesci.ucsb.edu (D.A.-A.), mzw@ucsb.edu (M.Z.W.)
https://doi.org/10.1016/j.cels.2023.06.001

SUMMARY

The integrated stress response (ISR) is a conserved signaling network that detects aberrations and computes cellular responses. Dissecting these computations has been difficult because physical and chemical inducers of stress activate multiple parallel pathways. To overcome this challenge, we engineered a photoswitchable control over the ISR sensor kinase PKR (opto-PKR), enabling virtual, on-target activation. Using light to control opto-PKR dynamics, we traced information flow through the transcriptome and for key downstream ISR effectors. Our analyses revealed a biphasic, proportional transcriptional response with two dynamic modes, transient and gradual, that correspond to adaptive and terminal outcomes. We then constructed an ordinary differential equation (ODE) model of the ISR, which demonstrated the dependence of future stress responses on past stress. Finally, we tested our model using high-throughput light-delivery to map the stress memory landscape. Our results demonstrate that cells encode information in stress levels, durations, and the timing between encounters.

A record of this paper's transparent peer review process is included in the supplemental information.

INTRODUCTION

The integrated stress response (ISR) is a conserved signaling network that allows cells to detect and react to cell-intrinsic and environmental stresses, including nutritional deficits, mitochondrial dysfunction, redox imbalances, viral infections, harmful RNA conformers, and mis-folded proteins in the endoplasmic reticulum (ER). Because of its fundamental nature, it is not surprising that dysregulation of the ISR has been implicated in the pathogenesis of our most widespread diseases, including diabetes, cancer, and neurodegeneration.[1] Four stress sensor kinases—PERK, PKR, HRI, and GCN2—actuate ISR signaling by phosphorylating a single serine of the α subunit of the eukaryotic translation initiation factor eIF2 (eIF2α), a heterotrimeric GTPase required for translation initiation. Phosphorylated eIF2α (p-eIF2α) competitively inhibits its guanine nucleotide exchange factor eIF2B,[2–4] which leads to a global shutdown of canonical translation. Concomitantly, phosphorylation of eIF2α promotes the translation of uORF-containing mRNAs, including those encoding the ISR effector transcription factors ATF4, CHOP, as well as GADD34, the regulatory subunit of protein-phosphatase 1 (PP1) that mediates negative feedback through dephosphorylation of eIF2α.[5–10] While the molecular structure and circuitry of the ISR in health and disease have been extensively studied,[1] major questions remain about how the ISR encodes information at the systems level. How does the intensity and duration of a stress determine the cell's response? On what timescales and with what subnetworks does the ISR determine cell fate? How do past stresses influence cellular resilience?

These questions are difficult to address with classical ISR-inducing agents such as chemicals (e.g., the ER calcium reuptake inhibitor thapsigargin[11] and sodium arsenite[12]), viral infection or synthetic RNAs (e.g., poly-I:C[13]), and physical stimuli such as heat shock because all of these stressors induce multiple parallel damage-response pathways that are conflated with molecular damage. Thus, bona fide changes in the cell's response to stress are difficult to disentangle from changes resulting due to failing cellular machinery. In addition, the dose-response relationship between real stressors and pathway activation is non-trivial because of the cascading failures that non-linearly alter cellular stress levels. Finally, damage induced by stressors is not immediately reversible. Instead, it must be

repaired by the cell, constraining the investigation of how the ISR decodes dynamic inputs.

An ideal approach for dissecting the ISR would have three properties. It would (1) isolate a single stress sensor and activate it virtually to avoid conflation of inputs from parallel pathways and molecular damage, (2) enable high-resolution input control to query input-output proportionality, and (3) exert precise control of recurrent stimulation dynamics to interrogate the relationship between past stresses and future ones.

Here, we develop an approach with exactly these properties, using an optogenetically engineered ISR kinase to dynamically stimulate the ISR pathway with "virtual stress." Optogenetic control enables the selective activation of a single kinase of the ISR pathway without inducing real molecular damage, greatly reducing the combinatorial complexity of the signals that are turned on by real stressors. By changing the intensity of light stimulation, it can tune the fraction of optogenetic proteins in the activated state, thereby precisely altering the perceived intensity. Light can also be quickly toggled on and off in a matter of milliseconds, enabling the delivery of precisely defined input dynamics. By assaying the global cellular changes in gene expression and the biochemical status at key protein nodes, such as eIF2α, in response to virtual stress of varying intensities and durations using high-throughput 96-well light delivery devices,[14] we can use optogenetic control to dissect the complex computations that govern the ISR pathway.

We apply our approach to the ISR kinase PKR, an innate immunity effector of vertebrates that detects viral and endogenous double-stranded RNA (dsRNA).[15–19] PKR signaling is dysregulated in numerous diseases, including cancer and neurodegenerative disorders,[20,21] illustrating its central role in maintaining organismal homeostasis. Thus, the interrogation of stress encoding and decoding through optical control of PKR has both a broad significance and specific implications for understanding the fundamental mechanisms cells use to respond to stress.

Although the role of ISR dynamics has not been systematically interrogated, observations suggest that it utilizes the modalities of dose and dynamics to encode a wide variety of cell states. PKR-induced ISR activity has been shown to stochastically pulse on the timescales of hours in response to viral infections, suggesting host-pathogen modulation of ISR dynamics.[22] More generally, the difference between an adaptive and a maladaptive stress response is commonly defined by the difference in dosage and timing of a stress input[23] (e.g., low, repeated doses of stress induce acclimation, whereas larger chronic doses cause physiological dysfunction). Both examples suggest that hysteresis, or history-dependent dynamics,[24] in the ISR may play a functional role in dictating outcomes.

To understand how the ISR decodes stress signaling features we systematically altered both the levels and dynamics of opto-PKR activity. We coupled these precise input control methods with quantitative, time-resolved analysis of global transcriptomic changes as well as single-cell measurements of individual ISR effectors. This strategy revealed transcriptome remodeling governed by two dynamical modes—transient and gradual—that are associated with adaptive and terminal ISR outcomes. By systematically varying virtual stress intensity, we determined that p-eIF2α, the adaptive transcription factor ATF4, and the pro-apoptotic transcription factor CHOP respond proportionally. We leveraged these insights to develop an ordinary differential equation (ODE) model which quantitatively predicted that both the duration of past stress and the recovery time after stress determine cellular stress memory. Experimental validation of this model mapped the landscape of cellular adaptation to stress.

RESULTS

Optogenetic activation of PKR induces the ISR

We chose to engineer optogenetic control over PKR for two reasons. First, PKR's activation mechanism involves high-order self-association,[25–27] which can be mimicked using optogenetic clustering tools. Second, PKR is cytoplasmically localized, and its sensor domain is isolated to a contiguous stretch of amino acids on the polypeptide chain, making it easier to engineer in comparison to the other ISR kinases.[28,29] Thus, we hypothesized that clustering PKR through exchanging PKR's dsRNA binding domains (dRBM1 and dRBM2) with photo-switchable variants of cryptochrome2 (Cry2), a light-inducible oligomerizer,[30] would result in light-based activation of the ISR (Figure 1A).

To construct optogenetic PKR (opto-PKR), we replaced dRBM1 and dRBM2 with one of three optimized variants of Cry2: Cry2Olig, Cry2OClust, and Cry2ODrop (Figures 1B and S1A). All three variants contain the E490G mutation in Cry2, which enhances the proteins' oligomerization efficiency and is commonly referred to as Cry2Olig.[31] In addition to this mutation, Cry2OClust and Cry2ODrop have C- and N-terminal peptide sequences, respectively, that increase their dynamic exchange with the cytoplasm[32,33] (Figure S1A). In this manner, Cry2Olig-PKR, Cry2OClust-PKR, and Cry2ODrop-PKR sample a range of biophysical assembly properties, from more solid-like to more liquid-like condensates.

To test whether our opto-PKR variants formed light-induced clusters, we transduced H4 neuroglioma cells and U2OS osteosarcoma cells, sorted them for expression-matched populations using fluorescence-activated cell sorting (Figure S1B), and took time-lapse images while continuously stimulating them with activating light. All three opto-PKR variants in both cell lines formed condensates demonstrating light-responsive clustering of the engineered proteins (Figures 1C, S1C, S1E, and S1F; Videos S1 and S2). We noted that the number and size of condensates rapidly increased and then declined for all opto-PKR constructs in both cell lines (Figures S1C–S1E). We additionally tested the Cry2Olig opto-PKR variant in non-cancerous HEK293T cells and found similar dynamics (Figure S1F; Video S2). An established point mutation (K296R) in the phosphate transfer site of the kinase domain of PKR[15] (Figure S1H) stabilized these clusters, indicating that their activation-induced dissolution requires kinase activity (Figure S1I; Video S3).

We next confirmed that none of the opto-PKR variants were constitutively activated in the dark and that illumination of wild-type (WT) H4 cells did not induce phosphorylation of either PKR or eIF2α (Figures S1I and S1J). We then measured the phosphorylation kinetics of engineered PKR (p-PKR), which we resolved on western blots by its higher molecular weight than endogenous PKR, and endogenous eIF2α (p-eIF2α) in response to continuous illumination. All opto-PKR variants rapidly induced high autophosphorylation (Figures 1D, 1E, S1K, and S1L), with similar activation levels and kinetics to classical ISR activators,

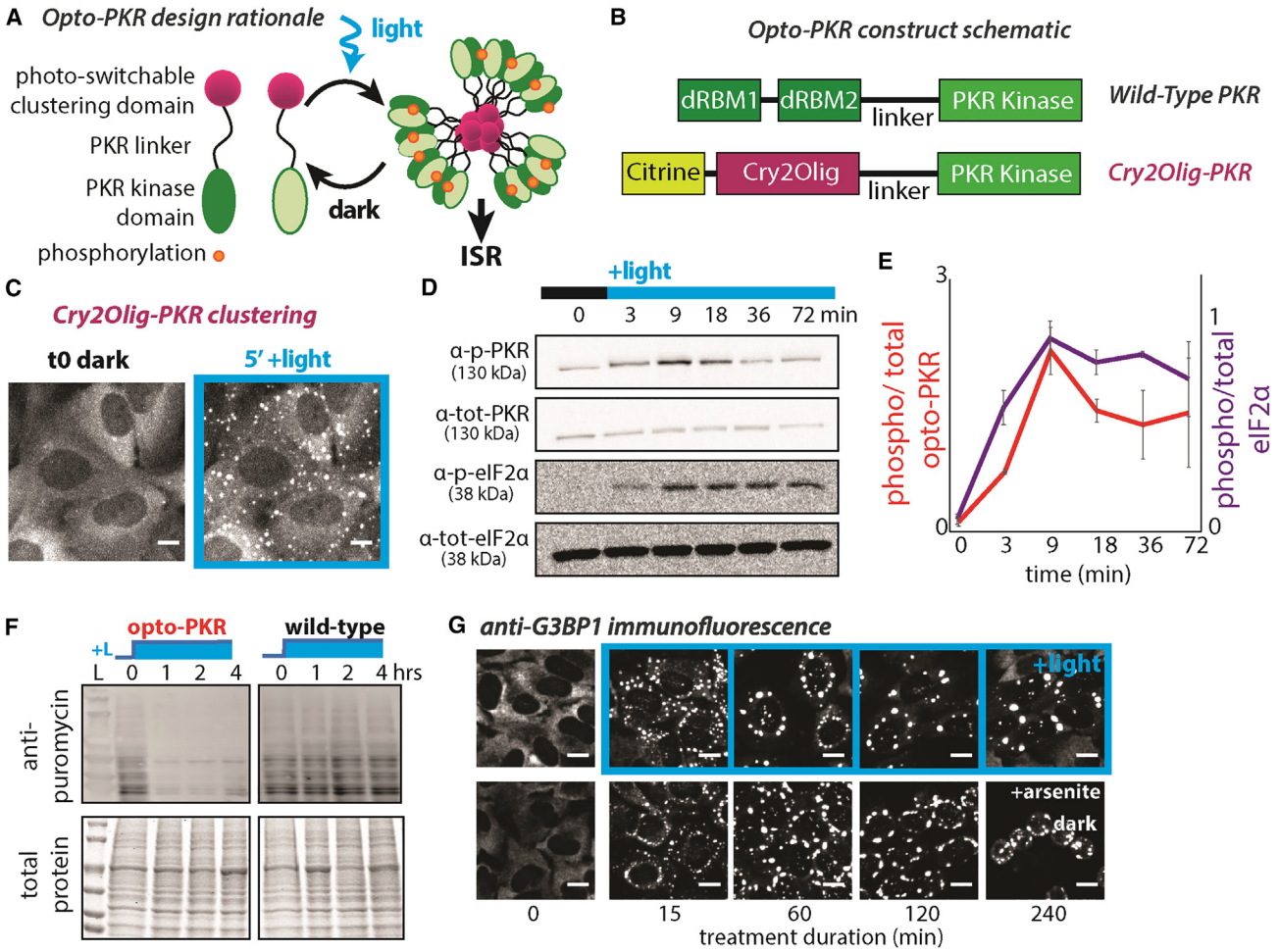

Figure 1. Optogenetic clustering of opto-PKR induces the canonical ISR

(A) Schematic representation of opto-PKR induction of ISR. Light-responsive Cry2 domain oligomerizes under blue light induction, leading to clustering and trans-autophosphorylation of the PKR domain with dark (no light) reversibility.

(B) Construct design and domains. Opto-PKR is a translational fusion between Cry2Olig and the PKR linker and kinase domain.

(C) Live cell imaging of opto-PKR in H4 cells activated under constant 450-nm illumination. Images are the maximum-intensity projection of 5 Z plans taken through the cell. Scale bars, 10 μm.

(D) Representative western blot of phosphorylated and total opto-PKR and eIF2α under continuous 450-nm illumination. Light treatment over 72 min. Illumination bar in black/blue above blots illustrates 450-nm illumination, with blue indicating illuminating conditions and black indicating dark conditions.

(E) Quantification of western blot in (D). Phosphorylation signal was calculated as the ratio of phosphorylated protein to total protein (PKR or eIF2α) at each time point. n = 3. Error bars represent SEM.

(F) Western blot of puromycin incorporation into proteins under blue light conditions in opto-PKR cells compared with the WT, illustrating light-activated translational attenuation. Light treatment over the period of 4 h. Note the strong translational repression elicited by the active opto-PKR.

(G) Immunofluorescence staining of stress granule marker G3BP1. Representative images of fixed opto-PKR cells activated through 450-nm illumination or in the dark with sodium arsenite (500 μM). Cells were stained for G3BP1. Note that arsenite induces cell death, while light does not. Scale bars, 10 μm.

arsenite and thapsigargin (Figure S1P). Given Cry2Olig-PKR's more consistent activation kinetics, we chose to work with this variant for the remainder of our experiments and refer to it as "opto-PKR" from here on.

Our initial continuous illumination experiments revealed receptor level negative feedback. We found that opto-PKR levels were reduced in response to light in all cell lines tested (Figures 1D and S1L–S1O). Thus, we performed a long-term illumination experiment with the proteasome inhibitor, MG-132, and the translation inhibitor, cycloheximide (CHX), to determine the cause of activation-induced receptor-level decreases (Figure S1Q). We found that neither translation inhibition nor proteasome inhibition alters the decay of active opto-PKR, leading us to conclude that the sensor is degraded through another mechanism, such as lysosomal proteolysis. However, CHX treatment increased the response duration of p-eIF2α (Figure S1Q), demonstrating the necessity of translation in determining p-eIF2α dynamics. Finally, we note that while receptor-level negative feedback did reduce levels of opto-PKR, it never becomes undetectable (Figure S1Q, *α-tot-PKR*), indicating that there is still an available pool of the receptor to encode long-duration stress inputs. Overall, the negative regulation on opto-PKR confirms previous reports that

activation induces a degradation of PKR[34] and suggests that history dependence in the ISR is dependent on both upstream- and downstream-acting negative feedback.

Finally, we sought to understand whether opto-PKR induced canonical cell physiological responses to stress: translation repression[35] and formation of stress granules (SGs), ribonucleoprotein complexes formed in response to stalled translational complexes.[36] To assess translational repression, we continuously activated opto-PKR and measured puromycin incorporation into nascent peptides using an anti-puromycin antibody.[37] Opto-PKR activation drastically reduced translation initiation, measured by nascent peptide puromycilation (Figure 1F), which is consistent with translational repression observed by ISR activation with chemical inducers.[38] Next, we monitored SG formation by immunofluorescence (IF) of the SG assembly factor G3BP1[39] upon activation of opto-PKR. Light-induced SGs, which did not co-localize with opto-PKR condensates, were indistinguishable from those formed through arsenite induction, except for those observed at late time points (>4 h), where arsenite-treated cells began to detach from the plate and die (Figures 1G and S1P–S1R). Altogether, our data demonstrate that opto-PKR recapitulates the major ISR events across multiple cell lines, allowing us to virtually control the ISR.

The stress-free ISR has a biphasic transcriptional response

Chemical ISR inducers have pleiotropic effects, rendering them ineffective tools to dissect the cellular responses to stress from cellular damage. To overcome this limitation, we used opto-PKR to globally characterize the dynamics of transcriptome remodeling in response to a "stress-free" ISR. We wondered whether distinct dynamic ISR phases might exist in response to virtual stress. Thus, we performed a time-resolved RNA sequencing (RNA-seq) experiment to characterize the dynamic changes in the transcriptome upon continuous stimulation with virtual stress. We utilized the optoPlate light delivery device,[14] which allows for arbitrary control over the illumination sequence of each well of a 96-well plate, to vary the duration of 450 nm light (~121 $\mu W/cm^2$, see STAR Methods for voltages) (Figure 2A). To obtain time-resolved transcriptional changes we sampled cells at 7 time points, from 0 to 12 h. Examination of individual markers of the ISR (e.g., *ATF3*, *DDIT3* [CHOP], *PPP1R15A* [GADD34], etc.) showed two distinct classes of dynamical responses corresponding with transiently pulsed and gradually accumulating mRNA kinetics (Figure S2A).

These two kinetic response classes suggested that the global transcriptome dynamics may also display a similar pattern. Thus, to map the global gene expression modes of the ISR, we performed a singular value decomposition on the *Z* scored, time-resolved transcriptome matrix (Figure 2A). This technique allowed us to re-project genes onto the orthogonal matrices that explain the most variance in the time domain. We found that the first two modes (σ_1 and σ_2) explained more than half of the total variance of the transcriptome (Figure 2B). To visualize these two dominant modes, we plotted the top 500 and bottom 500 genes from the U vectors associated with σ_1 and σ_2. This analysis showed that σ_1 represented a transient response, with genes reaching their maximum between 4 and 6 h of continuous activation (Figure 2C, top). On the other hand, genes represented by σ_2 showed a gradual but continuous change that leveled off between 8 and 10 h of illumination (Figure 2C, bottom). Analyzing the transcriptome separately through centroid clustering recapitulated these two dynamic modes (Figure 2D).

Gene ontology (GO) enrichment analysis of these modes hinted that transiently downregulated processes included translation, purine and carbohydrate metabolism, and gonadal mesoderm development, while transiently upregulated processes included protein ubiquitination and TGF-β signaling. This analysis suggests that the transient mode is associated with adaptive remodeling of the proteome and alteration of cell identity. On the other hand, gradually upregulated genes were associated with apoptosis and ER and nutrient stress responses, while gradually downregulated processes included mitosis and cell adhesion (Figure S2B). This analysis suggests that the gradual mode is associated with a switch toward a terminal response. Together, these results indicate that the ISR has two prominent dynamic modes—transient and gradual—and that these modes represent the adaptive and terminal responses of the ISR.

ISR transcription factors respond proportionally to inputs

The ISR culminates in gene expression programs controlled by adaptive (ATF4) and pro-apoptotic (CHOP) transcription factors, yet the question of how these transcription factors respond to varying the magnitude of a stress has remained unanswered. This question has been difficult to probe with chemical stressors because they induce cascading failures that can lead to a nonlinear relationship between chemical stressor concentration and ISR activity.[40] The ISR has been characterized to be switch-like in some instances,[7] while recent findings regarding the mechanism of action of ISR-inhibiting drugs (e.g., ISRIB) suggest a more nuanced dose-response relationship.[1,41,42] Thus, we wondered how the ISR signaling dynamics are affected by varying magnitudes of virtual stress inputs.

To this end, we characterized the dynamics, at the protein level, of p-eIF2α, ATF4, and CHOP, which represent the ISR core, and its adaptive and terminal phases, respectively (Figure 3A). To control the magnitude of virtual stress, we varied light intensity as it varies the proportion of Cry2 molecules in the photo-active state.[33] Using the optoPlate device, we applied light ranging from 4 to 121 $\mu W/cm^2$ for over 10 h (Figure S3A) and collected time points for IF analysis of p-eIF2α, ATF4, and CHOP to obtain their endogenous dynamic responses (Figure 3B). To analyze the IF images, we developed a custom image analysis pipeline that extracts single-cell fluorescence intensities from the nucleus, cytoplasm, and SGs, which we used to quantify the response in over 100 cells per condition for a total of more than 10,000 single cells across all times and intensities (Figures S3B and S3C).

In H4 cells, we found that the ISR nodes we examined had features that were modulated in proportion to their inputs. P-eIF2α peaked within 30 min of activation and then repressed by 4 h, with the peak magnitude varying in proportion to light intensity (Figures 3C and 3D). HEK293T cells also showed a proportional response (Figures S3D and S10). We found that ATF4 localized to SGs, similarly to sodium-arsenite-treated cells (Figure S3B), as has been reported previously.[43] SG-localized ATF4 peaked at 2 h of activation, where a subset of the adaptive response

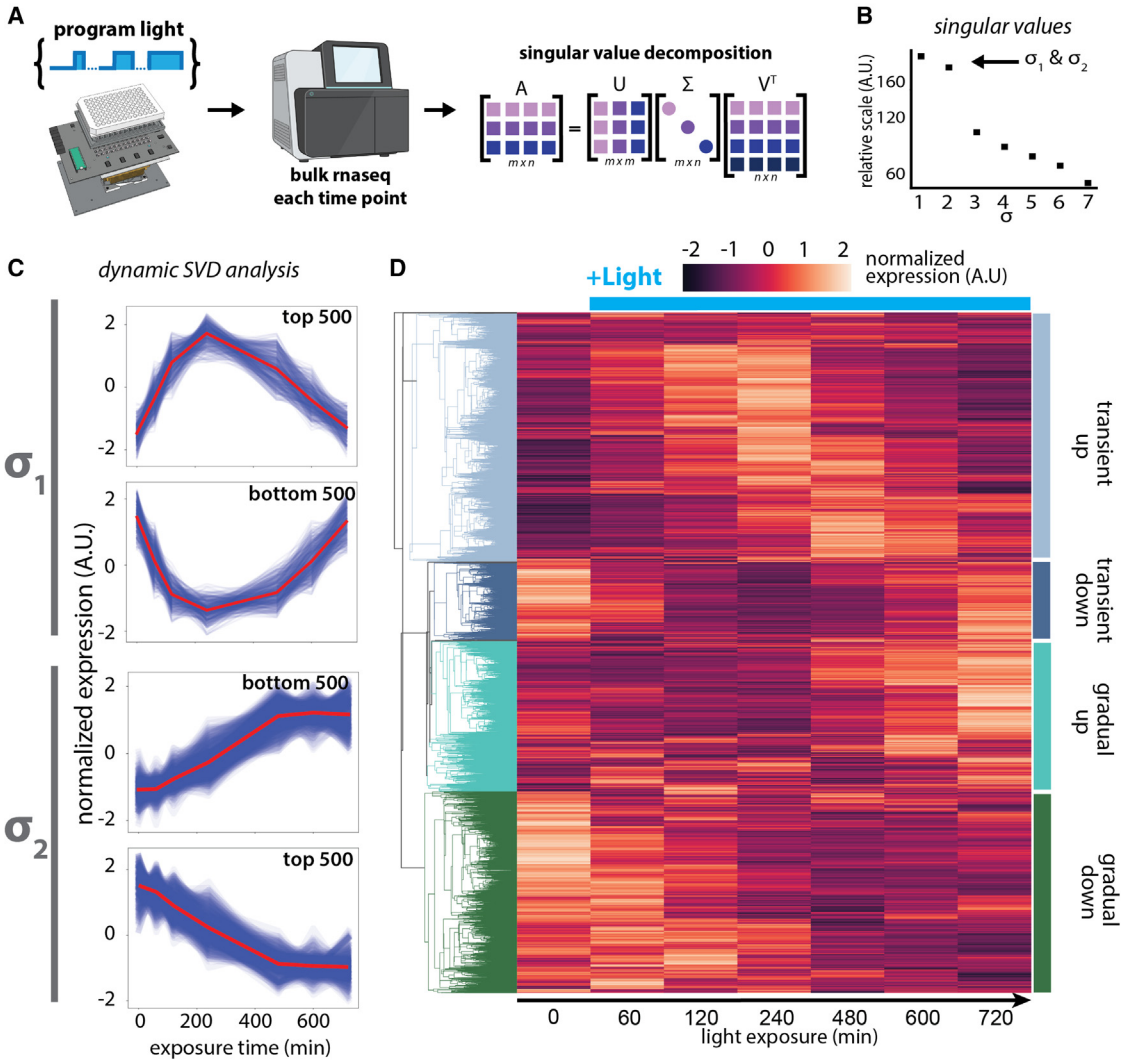

Figure 2. The ISR has a biphasic transcriptional response to virtual stress

(A) Experimental design. To investigate the transcriptomic dynamics of opto-PKR-induced ISR over time, H4 cells bearing opto-PKR were illuminated using the optoPlate device to collect 7 samples across 720 min.

(B) Plot of singular values from Σ matrix of singular value decomposition on a relative scale.

(C) Plot of the highest contributing 500 genes from transcriptome hits into the two dynamic modes (top and bottom) of σ_1 and σ_2. Each blue line represents a distinct gene from our *Z*-scored RNA-seq data, and the red line is the mean of 500 plotted genes over time. The *Z* score was normalized by taking every time point of each gene to its mean across all time points.

(D) Centroid-clustered heatmap of the global transcriptome dynamics over 12 h. Rooted tree diagram of gene clustering is color coded to indicate 4 dynamic modes.

genes peak (Figure S2A), with its peak height also proportional to the input (Figures 3E and 3F). We also noted a proportional response in the change in nuclear ATF4, although its magnitude was much lower than SG-localized ATF4 (Figure S3E). Finally, we found that CHOP accumulated gradually, with its rate of accumulation varying with the input intensity (Figures 3G and 3H).

We further probed the proportional intensity encoding of p-eIF2α and CHOP accumulation. We applied a smooth (256 bit) linear gradient of illumination across a field of opto-PKR cells. We then IF-stained for both p-eIF2α and CHOP, at times ranging from 0 to 12 h (Figures 3I and S3F). This graded illumination led to a spatially graded response in both p-eIF2α and CHOP (Figure 3I). Quantification of the data showed a best fit corresponding with a 2nd order polynomial, suggesting that the ISR has an accelerating behavior when computing p-eIF2α levels, which are then transmitted to CHOP protein levels (Figures 3J, S3G, and S3H). Overall, these experiments demonstrate that p-eIF2α, ATF4, and CHOP have a large dynamic range and are modulated in proportion to their inputs, albeit with a polynomial non-linearity.

A simple ODE model of the ISR captures core responses and predicts stress memory

Our studies so far have focused on probing the cellular response to continuous stress inputs. However, the ISR dynamically

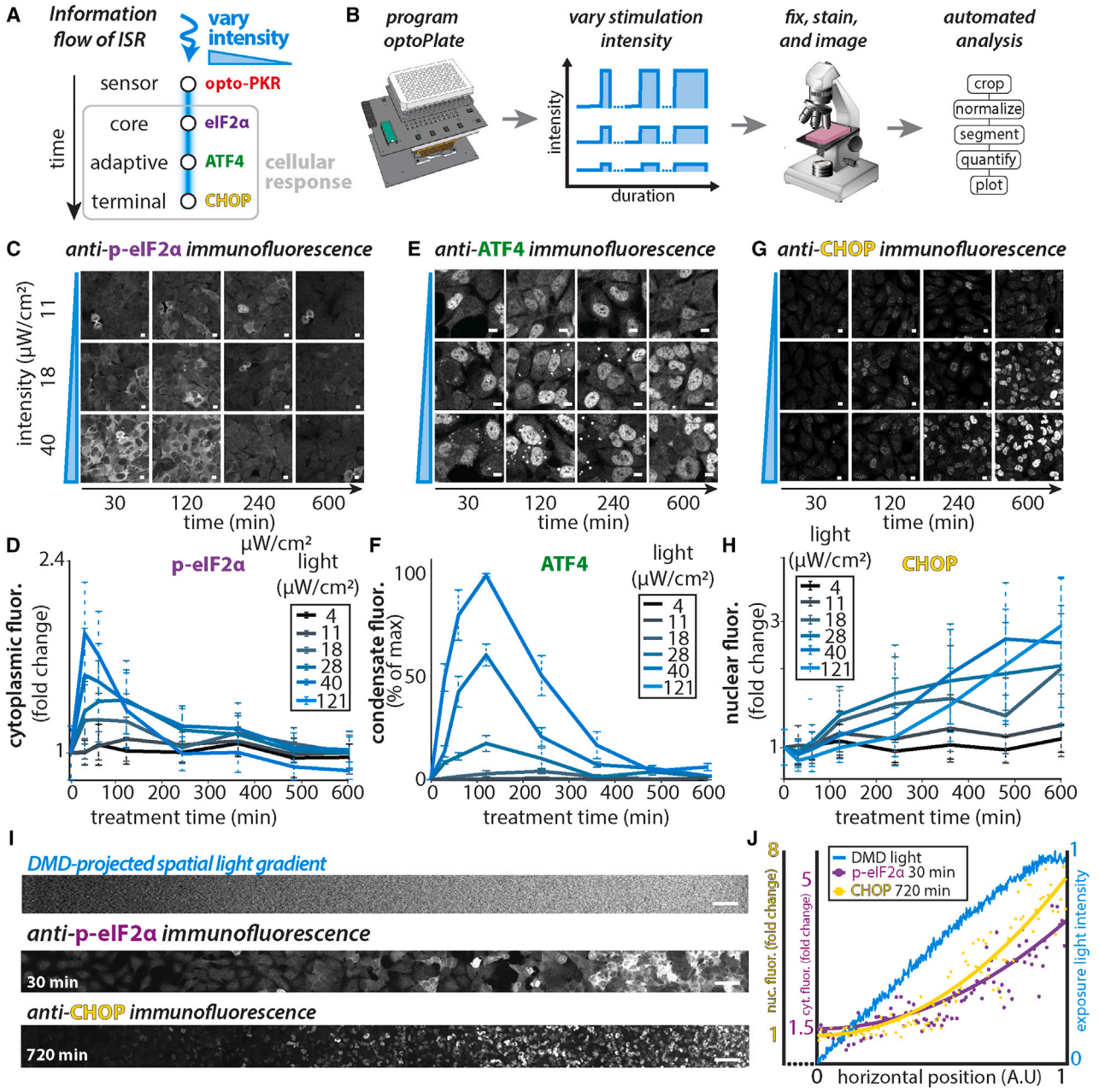

Figure 3. ISR transcription factors in different ISR signaling modes respond proportionally with fixed phases

(A) Schematic of ISR information flow through the activation of opto-PKR.

(B) Experimental design to query responses to varying illumination intensities over time. Blue light intensity was varied from 4 to 121 μW/cm^2 using the optoPlate device over a period of 600 min. Cells were fixed, immunostained for the indicated markers, and imaged, and immunofluorescence data were processed with an automated pipeline.

(C, E, and G) Representative immunofluorescence images of H4-opto-PKR cells under unique light exposures outlined, with varying combinations of intensity and duration and stained for p-eIF2α (C), ATF4 (E), and CHOP (G). Scale bars, 10 μm.

(D, F, and H) Quantification of immunofluorescence experiments (C, E, and G). Each line represents specific illumination intensity over time.

(D) Segmenting area around nucleus for cytoplasmic signal. n > 150 cells. Error bars represent standard deviation of population.

(F) Segmenting condensates, then taking total signal as a function of sum of all condensate intensity over number of cells. n > 40 cells per replicate. Error bars represent SEM of 3 separate technical replicates.

(H) Segmenting nuclei of each cell for nuclear signal. n > 150 cells. Error bars represent standard deviation of population.

(I) Representative immunofluorescence image of gradient light activation of H4-opto-PKR cells stained for p-eIF2α and CHOP. Light gradient applied through digital micro-mirror device (DMD) every 2 min. Scale bars, 100 μm.

(J) Quantification of cytoplasmic p-eIF2α and nuclear CHOP upon gradient light stimulation. Each point is mean nuclear immunofluorescence intensity of all nuclei positioned within one of the hundred equally divided horizontal space regions. Line of best fit adhering to quadratic formula: $f(x) = ax^2 + b$. n > 2,000.

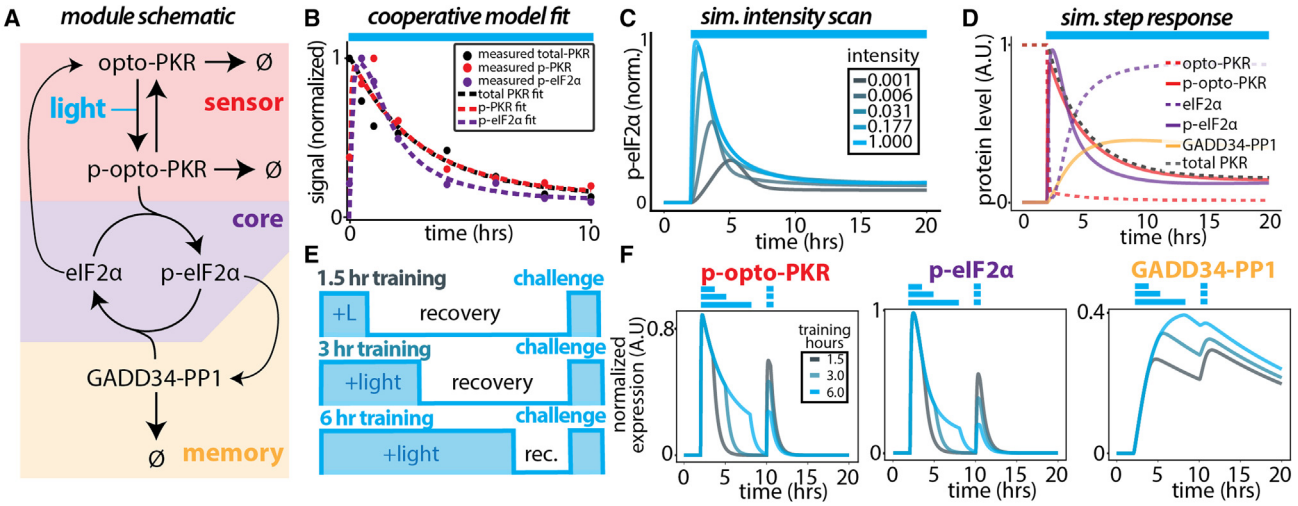

Figure 4. A simple ODE model of the ISR captures core responses and predicts stress memory

(A) Schematic representation of interactions simulated in our model using equations representing opto-PKR, p-opto-PKR, eIF2α, p-eIF2α, and GADD3-PP1 complex, segregated to three sub-modules of the ISR.

(B) Best fit of simulated data through cooperative ODE model to experimental data for total opto-PKR, p-opto-PKR, and p-eIF2α, where the line is simulated data and the points are experimentally measured data.

(C) Simulations showing changes in p-eIF2α levels in response to decreasing illumination intensity.

(D) Simulated response of all the state variables of our cooperative model after fitting to experimental data.

(E) Demonstration of inputs used to probe system hysteresis. To investigate the effect of past stress inputs to present stress inputs, we simulated multiple increasing ratios of stress inputs to recovery in the same period, before applying an identical challenge to all simulations.

(F) Simulated stress memory through the modulation of ratios of inputs to recovery. Normalized levels of key state variables over time: p-opto-PKR (left), p-eIF2α (mid), GADD34-PP1 (right). Challenge occurs at 10 h for all simulations.

oscillates in response to viral infection,[22] and the proposed adaptive effects of stress are inherently multi-phasic in that they describe the effect of past stresses on future ones.[44–46] To predict how dynamic stress inputs are processed, we constructed and fit a simple ODE model of the ISR. Although the ISR has been modeled before,[47] we sought to build the simplest model that still captured the system dynamics and to be the first to parameterize a model using non-damaging inputs, which could confound interpretations.

We chose to represent the ISR as three interconnected modules: sensor, core, and memory (Figure 4A). We approximate the sensor module, our ability to activate it with light, and its phosphorylation of eIF2α using mass action kinetics (Figure S4A). To minimize the number of free parameters, we simplified the core and memory modules by choosing to represent the guanosine diphosphate (GDP) and guanosine triphosphate (GTP)-bound forms of eIF2α, as well as the multiple eIF2B assembly states, as non-linear cooperative interactions between eIF2α, p-eIF2α, and the well-known phosphatase-coupling protein, GADD34 (Figures 4A and S4A). To parameterize our model, we fit it to the normalized p-opto-PKR, total opto-PKR, and p-eIF2α data collected for the maximal continuous activation (Figures 4B, S4B, and S4C). The model reproduced the receptor-level feedback on opto-PKR and GADD34 accumulation, as well as the observed modulation of peak p-eIF2α (Figures 4C and 4D; Method S1).

We hypothesized that both the background accumulation of effective PP1 activity in combination with the drop in opto-PKR levels would desensitize future inputs as a function of past inputs. To test this hypothesis, we simulated a short (1.5 h), intermediate (3 h), and long (6 h) stimulation followed by a uniform 30-min challenge, corresponding to the peak activation of the naive ISR (Figure 4E). These simulations demonstrated a negative relationship between the amount of prior stimulation on the ability of the core module of the ISR to respond to future challenges, which was mediated by the varying accumulation of GADD34-PP1 in the memory module, and the decrease in the available opto-PKR in the sensor module (Figures 4F and S4D). Overall, our model recapitulates the observed ISR dynamics and suggests that the ISR can encode memories of prior stimulations through modulating the concentration of PKR sensor and the activity of the GADD34-PP1 feedback control module, as has been recently suggested.[47]

Input dynamics shape the stress memory landscape

Chronically stressed cells respond differently than those exposed to acute stress,[48] suggesting a role for stress input duration in shaping the ISR. Our simulations predicted that prior inputs attenuate the system's response to future inputs, thus constituting a stress memory. To map the stress memory landscape, we varied the duration of stress input independently from the recovery duration. This stimulation/recovery regime was followed by a uniform challenge (10-min input) to query the cells' response (Figure 5A). Using our model (Method S1), we applied these variable training and recovery times to simulate the stress memory landscape. We found that the p-eIF2α was dependent on both conditioning variables (Figure 5B), anticorrelated with GADD34-PP1 levels at the time of challenge (Figure S5C) and correlated with the total

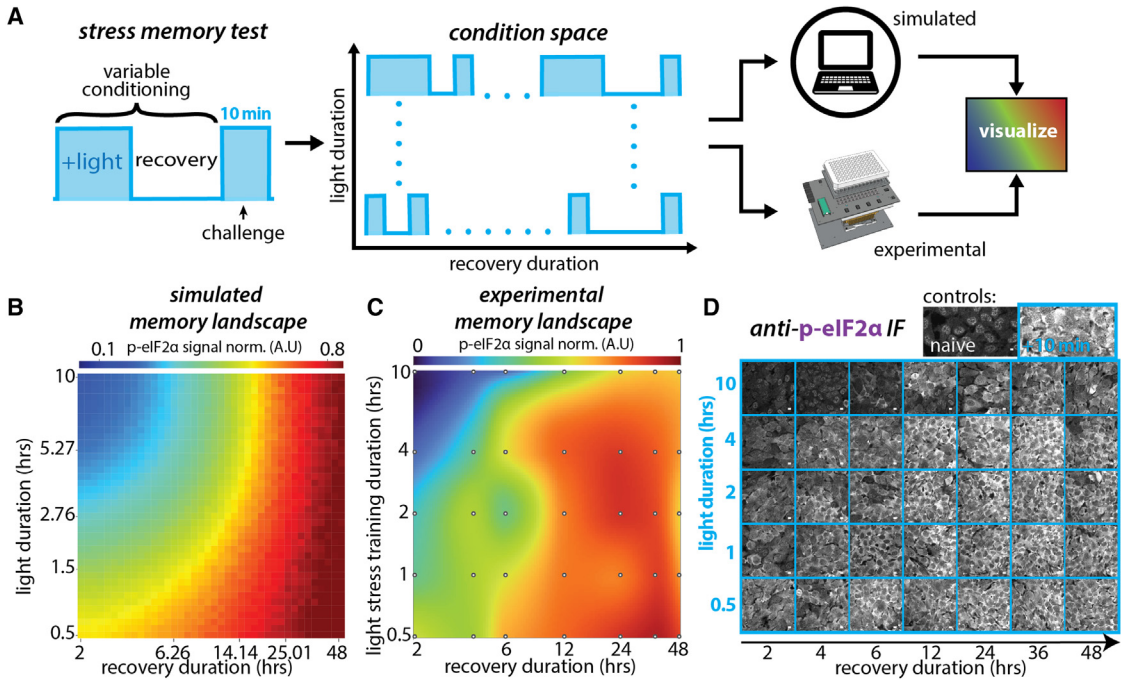

Figure 5. Input dynamics shape the stress memory landscape

(A) Experimental scheme used to map the stress memory landscape. Cells were conditioned by varying stress inputs and recovery durations, before applying an identical challenge to query present response. Conditioning inputs were applied to the cooperative model and to cells for comparison. Cells were illuminated with the optoPlate device, fixed, immunostained, and quantified for p-eIF2α (similarly to 3B).

(B) Heatmap of simulated stress memory landscape for p-eIF2α in response to 10-min challenge. Total duration of conditioning varies.

(C) Interpolated heatmap of experimental stress memory landscape for p-eIF2α in response to 10-min challenge. Input light intensity at 55 μW/cm^2. Experimental data quantified as normalized mean intensity of cytoplasmic immunofluorescence signal. Each dot represents a sample point. n > 375 single cells for each point.

(D) Representative immunofluorescence images immunostained for p-eIF2α after conditioning and challenge. Controls: naive, no illumination, +10 min, only challenge (no conditioning). Scale bars, 10 μm.

opto-PKR (Figure S5D). Notably, the response of the ISR to the fixed challenge in simulations that were trained with long durations of stress (~3–10 h), but given short recovery times (<7 h), was severely blunted (Figure 5B).

To test whether our model predicted the stress memory landscape, we used the optoPlate device to probe the response to a subset of the conditioning inputs, followed by the same 10-min challenge. These experiments require rapid reversibility of the stimulus to ensure that the queried cellular state is only a response to the most recent challenge and not the continuation of a previous activation. Therefore, we measured the phosphorylation decay of p-eIF2α in response to pulses of activating light of varying durations and found that it decayed on the timescale of 30 min at all tested durations of activation, significantly faster than the briefest recovery duration tested (2 h) (Figure S5A). We note that by testing the decay in response to longer duration inputs, we ensured that the system is not locked into a light active state, even upon withdrawal of activating light. In addition, we verified that p-eIF2α is inactive prior to the 10-min challenge (Figure S5B), with only scattered p-eIF2α activity in dividing cells, as has been reported previously.[49] Finally, we confirmed with our model and previous experiments that opto-PKR is still present after input durations > 7 h (Figures 1F, 4B, and S1Q).

We found that our model predictions were in agreement with the cellular response. Long duration inputs and short recovery times severely blunted p-eIF2α levels (Figure 5C). Short duration inputs also reduced p-eIF2α levels, whereas cells were generally fully recovered after >12 h (Figure 5C). Upon examination of IF images, we found these patterns were visibly evident (Figure 5D). Finally, we co-stained for the SG marker, G3BP1, and found that only after the longest-duration inputs, corresponding to peak terminal phase, did cells completely inhibit SG formation (Figure S5D). Together, our simulations and experimental data describe the timescales of cellular adaptation to stress and implicate downstream negative feedback (e.g., GADD34) and upstream receptor-level feedback in determining the memory landscape.

DISCUSSION

Neuronal optogenetic tools revolutionized neuroscience because of their ability to causally dissect the role of neural firing dynamics in driving a brain or behavior state. Here, we use cellular optogenetic tools analogously to control the perceived ISR input and understand how ISR signaling dynamics dictate cellular outcomes. The ability to deliver ISR input dynamics without damaging cells—we call this virtual stress—allowed us to address three longstanding questions: (1) What are the temporal phases of the ISR? (2) How do these responses relate to stress intensities? (3) How is the ISR modified by its history?

Based on our analysis of time-resolved transcriptomic profiling, we propose that the ISR can be delineated into two distinct dynamical modes: (1) a transient mode associated with the pro-adaptive response that peaks at ~4 h and (2) a gradual mode that slowly activates terminal response genes in the background, leveling off at ~10 h. Using this insight, we probed pathway encoding at key nodes, representative of the gradual and transient phases, by coupling a high-throughput light delivery device to custom automated image analysis algorithms. This approach allowed us to systematically scan through activation levels and durations in thousands of single cells, revealing that they respond proportionally to stress levels, albeit with their own phase-dependent dynamics. We found that the timing of these two phases was unchanged by intensity, suggesting that stress duration is a central feature sensed by the ISR. A detailed analysis of the effects of stress intensity on the dynamics of the transcriptome remains an important future direction.

Our data guided us to construct a simple ODE model of the ISR to explore its dynamical properties. We found that the model displays hysteresis, which suggested that it could be used to predict the encoding of stress memories. By systematically modeling variations in the duration of both stress input as well as recovery time, we simulated a stress memory landscape that predicted that longer stresses and shorter recovery times generally blunt the cell's present response. We validated our model's prediction experimentally, generating the first map of the stress memory landscape. Our model highlights the combination of receptor-level degradation and phosphatase-induced negative feedback shaping this memory landscape. Rather than focusing solely on cellular contexts where stress is delivered in a sustained manner using small molecule poisons, our work points to the importance of pulsatile and/or stochastic ISR dynamics that have now been observed to occur in response to viral infection.[47]

The value of "virtual" stress in interrogating pathways that detect molecular damage

Virtually activating the ISR allowed us to systematically screen through fixed intensities of perceived stress, making way for the analysis of a stress-free ISR. This allowed us to examine the global transcriptomic state of cells without confounding alterations due to failing cellular subroutines (such as a damaged ER resulting from thapsigargin treatment[11] or sublethal oxidation arising from arsenite exposure[12]). By isolating a single sensor, PKR, our approach also allows us to eliminate any possible contributions of parallel stress response pathways that are activated by the same input, as occurs with multiple innate immunity dsRNA sensors.[50] Despite continuously activating the ISR for over 16 h, we did not observe significant signs of cell death in the cell lines we studied. This could be explained by one of the following scenarios: (1) the cancer cells have re-wired their stress response to avoid or actively suppress apoptosis; (2) in certain cell types, ISR-induced programmed cell death requires additional inputs, which are satisfied by true damage; or (3) cell death requires longer chronic ISR induction than that was tested in this study. Indeed, GO analysis of the terminal phase showed that apoptotic processes (GO: 0006915) were significantly enriched in the upregulated gene class, indicating a potential preamble to ISR-induced apoptosis. Furthermore, studies of how the ISR is re-wired across a range of cancers using orthogonally controlled stress sensors such as ours could reveal how oncogenic transformation selects for genotypic and epigenetic states that curb ISR-induced cell death.

An additional advantage of optogenetic induction over traditional stressors is that it can be patterned arbitrarily in space through the spatial modulation of light. We used this property to probe the decoding function of CHOP. Using digital micromirror devices with 256-bit resolution, we delivered a linear gradient of light to smoothly modulate the ratio of opto-PKR molecules in the photo-active and photo-inactive states. Cells produced a shallow 2nd order quadratic response in their p-eIF2α and CHOP protein levels, suggesting that cells detect a wide range of stress intensities at these key nodes.

The effect of long duration stimuli on PKR activation

Long duration inputs to opto-PKR indicate an apparent contradiction. On the one hand, both western blot and IF data (Figures 1, 3, and S1Q) show that opto-PKR degrades to a minimal level over the duration of 2–4 h. This receptor-level degradation, in combination with other downstream negative feedback regulators (e.g., GADD34), explains a concomitant drop in p-eIF2α levels on a similar timescale (Figure 1Q). On the other hand, in our stress memory experiments, we show that increasing the light duration beyond 4 h continues to affect the ISR memory in terms of p-eIF2α response (Figures 5C and 5D). These lead to the apparent contradiction that stimulation of opto-PKR influences the ISR long after it has been degraded.

We refer to our western blots and computational model to explain this contradiction. We find that although the pool of available opto-PKR drops, it never goes to zero, and a basal level is maintained (Figures 4B, 4F [left] and S1Q). Our model demonstrates that this is because additional opto-PKR continues being produced as GADD34 levels increase. This downstream negative feedback alleviates translational attenuation (Figure 1F) enough to induce basal expression of the receptor and thereby resolve the contradiction. We note that our global transcriptomic analysis (Figure 2) showed a cluster of genes that continue to respond to illumination well beyond the initial transient response. These genes constitute a potential mechanism for the cell to log the duration of ISR activation for cellular decisions that are induced in response to chronic inputs. Overall, these observations highlight the intricate interplay between feedbacks on different nodes in the pathway and suggest potential mechanisms for altering the cellular response to chronic stress by, for example, modulating the relative strength and timing of upstream and downstream feedback on the ISR.

The stress memory landscape in terms of normal cellular functions, adaptation, and stress-related diseases

Our model and experiments not only make quantitative predictions but also suggest where stress memory is stored and what parameters should be modified to alter the shape of the stress memory landscape. Our simulations demonstrate that the instantaneous level of the GADD34-PP1 complex and the availability of stress sensor kinases are, at least in part, responsible for the ISR's history-dependence (Figures 4E, 4F, and S4D). However, at least another PP1 regulatory subunit, CreP, also

induces dephosphorylation of eIF2α outside the negative feedback loop established by the induction of GADD34 and should be accounted for in further evaluation of stress memories. We found that stress memory is a combination of feedback on upstream and downstream components. As such, altering the parameters of effective GADD34-PP1 (K, K_1, K_2, and $ß_1$) and its degradation ($ß_2$), as well as the creation and degradation of the sensor (α_0, δ_1), will enable manipulation of the memory landscape. While the rates of accumulation and decay of GADD34 and PKR explain, to some degree, the encoding of stress memories (this work and Klein et al.[47]), we cannot discard the possibility that other regulators of the availability of ternary complex (i.e., CreP, eIF2B) could also contribute to the stress memory landscape. Drugs targeting these parameters may prove to be useful in alleviating disease symptoms caused by failure of the cell to either forget or remember past stresses. Further *in vivo* studies will be required to address this possibility.

In healthy cells challenged with short durations of stress, the ISR induces an adaptive response that increases resilience. On the other hand, this same pathway, when chronically activated, causes disease marked by reduced cellular function and increased cell death.[20] Because the severity and likelihood of onset of many ISR-related diseases (e.g., Alzheimer's, Huntington's, Parkinson's, and diabetes) increases with age, this observation begs the question of whether the ISR's dynamical information processing capability is prone to corruption during aging. Recently, the role of altered signaling dynamics was shown to explain how some cancers misperceive extracellular signals, transmuting healthy dynamical information into oncogenic signals.[51] Whether altered ISR dynamics explain disease states in a similar manner, with age-related changes in the ISR network altering the healthy cellular perception of stress, remains an open question. Future studies combining precise optogenetic stimuli with live-cell fluorescent reporters of canonical stress-responding nodes, such as fluorescent protein CRISPR-tagged ATF4 and CHOP, in models of ISR-associated diseases may illuminate this question.

STAR★METHODS

Detailed methods are provided in the online version of this paper and include the following:

- KEY RESOURCES TABLE
- RESOURCE AVAILABILITY
  - Lead Contact
  - Materials availability
  - Data and code availability
- EXPERIMENTAL MODEL AND STUDY PARTICIPANT DETAILS
  - Cell culture
- METHOD DETAILS
  - DNA constructs
  - Lentivirus transduction
  - Fluorescence activated cell sorting
  - Western blotting
  - Puromycilation of nascent peptides
  - Immunofluorescence
  - Microscopy imaging
  - Optogenetic stimulation
  - Image analysis
  - Bulk RNAseq
  - Simulating the mathematical model of ISR
  - Gene ontology analysis

SUPPLEMENTAL INFORMATION

Supplemental information can be found online at https://doi.org/10.1016/j.cels.2023.06.001.

ACKNOWLEDGMENTS

We thank Carmella Sidrauski and the members of her lab for insightful discussions, Charles E. Samuel for kind and helpful advice, Kelly Heom for training and assistance with RNA-seq, Jared Toettcher for lentiviral packaging plasmids, and the members of the D. Acosta-Alvear and M.Z. Wilson labs for critical discussions. This study was supported by UCSB start-up funds and the structured research agreement from Calico Life Sciences LLC.

AUTHOR CONTRIBUTIONS

Conceptualization, T.B., D.A.-A., and M.Z.W.; methodology, T.B., F.Z., D.A.-A., and M.Z.W.; software and data analysis, T.B. and M.Z.W.; modeling and simulations, M.Z.W.; investigation, T.B., R.A.P., and R.J.G.; resources, S.S.D., D.A.-A., and M.Z.W.; writing – original draft, T.B. and M.Z.W.; editing – final draft, T.B., F.Z., D.A.-A., and M.Z.W.; funding acquisition, D.A.-A. and M.Z.W.

DECLARATION OF INTERESTS

M.Z.W. is an employee, shareholder, and board member of Integrated Biosciences Inc.; T.B. is an employee of Integrated Biosciences Inc.; D.A.-A. is an employee of Altos Labs; and F.Z. is an employee of Altos Labs.

INCLUSION AND DIVERSITY

We support inclusive, diverse, and equitable conduct of research.

Received: June 13, 2022
Revised: December 27, 2022
Accepted: June 9, 2023
Published: July 19, 2023

REFERENCES

1. Costa-Mattioli, M., and Walter, P. (2020). The integrated stress response: from mechanism to disease. Science *368*. https://doi.org/10.1126/science.aat5314.
2. Krishnamoorthy, T., Pavitt, G.D., Zhang, F., Dever, T.E., and Hinnebusch, A.G. (2001). Tight binding of the phosphorylated alpha subunit of initiation factor 2 (eIF2alpha) to the regulatory subunits of guanine nucleotide exchange factor eIF2B is required for inhibition of translation initiation. Mol. Cell. Biol. *21*, 5018–5030.
3. Kashiwagi, K., Yokoyama, T., Nishimoto, M., Takahashi, M., Sakamoto, A., Yonemochi, M., Shirouzu, M., and Ito, T. (2019). Structural basis for eIF2B inhibition in integrated stress response. Science *364*, 495–499.
4. Adomavicius, T., Guaita, M., Zhou, Y., Jennings, M.D., Latif, Z., Roseman, A.M., and Pavitt, G.D. (2019). The structural basis of translational control by eIF2 phosphorylation. Nat. Commun. *10*, 2136.
5. Harding, H.P., Novoa, I., Zhang, Y., Zeng, H., Wek, R., Schapira, M., and Ron, D. (2000). Regulated translation initiation controls stress-induced gene expression in mammalian cells. Mol. Cell *6*, 1099–1108.
6. Lu, P.D., Harding, H.P., and Ron, D. (2004). Translation reinitiation at alternative open reading frames regulates gene expression in an integrated stress response. J. Cell Biol. *167*, 27–33.

7. Vattem, K.M., and Wek, R.C. (2004). Reinitiation involving upstream ORFs regulates ATF4 mRNA translation in mammalian cells. Proc. Natl. Acad. Sci. USA *101*, 11269–11274.

8. Palam, L.R., Baird, T.D., and Wek, R.C. (2011). Phosphorylation of eIF2 facilitates ribosomal bypass of an inhibitory upstream ORF to enhance CHOP translation. J. Biol. Chem. *286*, 10939–10949.

9. Lee, Y.Y., Cevallos, R.C., and Jan, E. (2009). An upstream open reading frame regulates translation of GADD34 during cellular stresses that induce eIF2alpha phosphorylation. J. Biol. Chem. *284*, 6661–6673.

10. Novoa, I., Zeng, H., Harding, H.P., and Ron, D. (2001). Feedback inhibition of the unfolded protein response by GADD34-mediated dephosphorylation of eIF2alpha. J. Cell Biol. *153*, 1011–1022.

11. Thastrup, O., Cullen, P.J., Drøbak, B.K., Hanley, M.R., and Dawson, A.P. (1990). Thapsigargin, a tumor promoter, discharges intracellular Ca2+ stores by specific inhibition of the endoplasmic reticulum Ca2(+)-ATPase. Proc. Natl. Acad. Sci. USA *87*, 2466–2470.

12. Lowenstein, D.H., Chan, P.H., and Miles, M.F. (1991). The stress protein response in cultured neurons: characterization and evidence for a protective role in excitotoxicity. Neuron *7*, 1053–1060.

13. Tamassia, N., Le Moigne, V., Rossato, M., Donini, M., McCartney, S., Calzetti, F., Colonna, M., Bazzoni, F., and Cassatella, M.A. (2008). Activation of an immunoregulatory and antiviral gene expression program in poly(I:C)-transfected human neutrophils. J. Immunol. *181*, 6563–6573.

14. Bugaj, L.J., and Lim, W.A. (2019). High-throughput multicolor optogenetics in microwell plates. Nat. Protoc. *14*, 2205–2228.

15. Thomis, D.C., and Samuel, C.E. (1993). Mechanism of interferon action: evidence for intermolecular autophosphorylation and autoactivation of the interferon-induced, RNA-dependent protein kinase PKR. J. Virol. *67*, 7695–7700.

16. Chung, H., Calis, J.J.A., Wu, X., Sun, T., Yu, Y., Sarbanes, S.L., Dao Thi, V.L., Shilvock, A.R., Hoffmann, H.H., Rosenberg, B.R., et al. (2018). Human ADAR1 prevents endogenous RNA from triggering translational shutdown. Cell *172*, 811–824.e14.

17. Kim, Y., Park, J., Kim, S., Kim, M., Kang, M.G., Kwak, C., Kang, M., Kim, B., Rhee, H.W., and Kim, V.N. (2018). PKR senses nuclear and mitochondrial signals by interacting with endogenous double-stranded RNAs. Mol. Cell *71*, 1051–1063.e6.

18. Youssef, O.A., Safran, S.A., Nakamura, T., Nix, D.A., Hotamisligil, G.S., and Bass, B.L. (2015). Potential role for snoRNAs in PKR activation during metabolic stress. Proc. Natl. Acad. Sci. USA *112*, 5023–5028.

19. Ben-Asouli, Y., Banai, Y., Pel-Or, Y., Shir, A., and Kaempfer, R. (2002). Human interferon-gamma mRNA autoregulates its translation through a pseudoknot that activates the interferon-inducible protein kinase PKR. Cell *108*, 221–232.

20. Martinez, N.W., Gómez, F.E., and Matus, S. (2021). The potential role of protein kinase R as a regulator of age-related neurodegeneration. Front. Aging Neurosci. *13*, 638208.

21. Gal-Ben-Ari, S., Barrera, I., Ehrlich, M., and Rosenblum, K. (2018). PKR: a kinase to remember. Front. Mol. Neurosci. *11*, 480.

22. Ruggieri, A., Dazert, E., Metz, P., Hofmann, S., Bergeest, J.P., Mazur, J., Bankhead, P., Hiet, M.S., Kallis, S., Alvisi, G., et al. (2012). Dynamic oscillation of translation and stress granule formation mark the cellular response to virus infection. Cell Host Microbe *12*, 71–85.

23. Murray, K.O., Clanton, T.L., and Horowitz, M. (2022). Epigenetic responses to heat: from adaptation to maladaptation. Exp. Physiol. *107*, 1144–1158. https://doi.org/10.1113/EP090143.

24. Strogatz, S.H. (1994). Nonlinear Dynamics and Chaos: With Applications to Physics, Biology, Chemistry, and Engineering (Studies in Nonlinearity) (CRC Press).

25. Zappa, F., Muniozguren, N.L., Ponce-Rojas, J.C., and Acosta-Alvear, D. (2022). Signaling by the integrated stress response kinase PKR is fine-tuned by dynamic clustering. J. Cell Biol. *221*, e202111100. https://doi.org/10.1101/2021.11.21.469455.

26. Mayo, C.B., Erlandsen, H., Mouser, D.J., Feinstein, A.G., Robinson, V.L., May, E.R., and Cole, J.L. (2019). Structural basis of protein kinase R autophosphorylation. Biochemistry *58*, 2967–2977.

27. Corbet, G.A., Burke, J.M., Bublitz, G.R., and Parker, R. (2022). dsRNA-induced condensation of antiviral proteins promotes PKR activation. J. Biol. Chem. *295*, 1426–1438. https://doi.org/10.1101/2022.01.14.476399.

28. Zhu, S., Romano, P.R., and Wek, R.C. (1997). Ribosome targeting of PKR is mediated by two double-stranded RNA-binding domains and facilitates in vivo phosphorylation of eukaryotic initiation factor-2. J. Biol. Chem. *272*, 14434–14441.

29. Cole, J.L. (2007). Activation of PKR: an open and shut case? Trends Biochem. Sci. *32*, 57–62.

30. Bugaj, L.J., Choksi, A.T., Mesuda, C.K., Kane, R.S., and Schaffer, D.V. (2013). Optogenetic protein clustering and signaling activation in mammalian cells. Nat. Methods *10*, 249–252.

31. Taslimi, A., Vrana, J.D., Chen, D., Borinskaya, S., Mayer, B.J., Kennedy, M.J., and Tucker, C.L. (2014). An optimized optogenetic clustering tool for probing protein interaction and function. Nat. Commun. *5*, 4925.

32. Park, H., Kim, N.Y., Lee, S., Kim, N., Kim, J., and Heo, W.D. (2017). Optogenetic protein clustering through fluorescent protein tagging and extension of CRY2. Nat. Commun. *8*, 30.

33. Shin, Y., Berry, J., Pannucci, N., Haataja, M.P., Toettcher, J.E., and Brangwynne, C.P. (2017). Spatiotemporal control of intracellular phase transitions using light-activated optoDroplets. Cell *168*, 159–171.e14.

34. Zappa, F., Muniozguren, N.L., Wilson, M.Z., Costello, M.S., Ponce-Rojas, J.C., and Acosta-Alvear, D. (2022). Signaling by the integrated stress response kinase PKR is fine-tuned by dynamic clustering. J. Cell Biol. *221*. https://doi.org/10.1083/jcb.202111100.

35. Dever, T.E., Feng, L., Wek, R.C., Cigan, A.M., Donahue, T.F., and Hinnebusch, A.G. (1992). Phosphorylation of initiation factor 2 alpha by protein kinase GCN2 mediates gene-specific translational control of GCN4 in yeast. Cell *68*, 585–596.

36. Buchan, J.R., and Parker, R. (2009). Eukaryotic stress granules: the ins and outs of translation. Mol. Cell *36*, 932–941.

37. Schmidt, E.K., Clavarino, G., Ceppi, M., and Pierre, P. (2009). SUnSET, a nonradioactive method to monitor protein synthesis. Nat. Methods *6*, 275–277.

38. Dey, S., Baird, T.D., Zhou, D., Palam, L.R., Spandau, D.F., and Wek, R.C. (2010). Both transcriptional regulation and translational control of ATF4 are central to the integrated stress response. J. Biol. Chem. *285*, 33165–33174.

39. Kedersha, N., Panas, M.D., Achorn, C.A., Lyons, S., Tisdale, S., Hickman, T., Thomas, M., Lieberman, J., McInerney, G.M., Ivanov, P., et al. (2016). G3BP-Caprin1-USP10 complexes mediate stress granule condensation and associate with 40S subunits. J. Cell Biol. *212*, 845–860.

40. Pakos-Zebrucka, K., Koryga, I., Mnich, K., Ljujic, M., Samali, A., and Gorman, A.M. (2016). The integrated stress response. EMBO Rep. *17*, 1374–1395.

41. Zyryanova, A.F., Weis, F., Faille, A., Alard, A.A., Crespillo-Casado, A., Sekine, Y., Harding, H.P., Allen, F., Parts, L., Fromont, C., et al. (2018). Binding of ISRIB reveals a regulatory site in the nucleotide exchange factor eIF2B. Science *359*, 1533–1536.

42. Tsai, J.C., Miller-Vedam, L.E., Anand, A.A., Jaishankar, P., Nguyen, H.C., Renslo, A.R., Frost, A., and Walter, P. (2018). Structure of the nucleotide exchange factor eIF2B reveals mechanism of memory-enhancing molecule. Science *359*. https://doi.org/10.1126/science.aaq0939.

43. Mateju, D., Eichenberger, B., Voigt, F., Eglinger, J., Roth, G., and Chao, J.A. (2020). Single-molecule imaging reveals translation of mRNAs localized to stress granules. Cell *183*, 1801–1812.e13.

44. Calabrese, E.J., Bachmann, K.A., Bailer, A.J., Bolger, P.M., Borak, J., Cai, L., Cedergreen, N., Cherian, M.G., Chiueh, C.C., Clarkson, T.W., et al. (2007). Biological stress response terminology: integrating the concepts

of adaptive response and preconditioning stress within a hormetic dose-response framework. Toxicol. Appl. Pharmacol. *222*, 122–128.

45. Calabrese, E.J., and Calabrese, V. (2022). Enhancing health span: muscle stem cells and hormesis. Biogerontology *23*, 151–167.
46. Ost, M., Coleman, V., Kasch, J., and Klaus, S. (2016). Regulation of myokine expression: role of exercise and cellular stress. Free Radic. Biol. Med. *98*, 78–89.
47. Klein, P., Kallenberger, S.M., Roth, H., Roth, K., Ly-Hartig, T.B.N., Magg, V., Aleš, J., Talemi, S.R., Qiang, Y., Wolf, S., et al. (2022). Temporal control of the integrated stress response by a stochastic molecular switch. Sci. Adv. *8*, eabk2022.
48. Guan, B.J., van Hoef, V., Jobava, R., Elroy-Stein, O., Valasek, L.S., Cargnello, M., Gao, X.H., Krokowski, D., Merrick, W.C., Kimball, S.R., et al. (2017). A unique ISR program determines cellular responses to chronic stress. Mol. Cell *68*, 885–900.e6.
49. Kim, Y., Lee, J.H., Park, J.E., Cho, J., Yi, H., and Kim, V.N. (2014). PKR is activated by cellular dsRNAs during mitosis and acts as a mitotic regulator. Genes Dev. *28*, 1310–1322.
50. Hur, S. (2019). Double-stranded RNA sensors and modulators in innate immunity. Annu. Rev. Immunol. *37*, 349–375.
51. Bugaj, L.J., Sabnis, A.J., Mitchell, A., Garbarino, J.E., Toettcher, J.E., Bivona, T.G., and Lim, W.A. (2018). Cancer mutations and targeted drugs can disrupt dynamic signal encoding by the Ras-Erk pathway. Science *361*. https://doi.org/10.1126/science.aao3048.
52. Schneider, C.A., Rasband, W.S., and Eliceiri, K.W. (2012). NIH Image to ImageJ: 25 years of image analysis. Nat. Methods *9*, 671–675.
53. Hashimshony, T., Senderovich, N., Avital, G., Klochendler, A., de Leeuw, Y., Anavy, L., Gennert, D., Li, S., Livak, K.J., Rozenblatt-Rosen, O., et al. (2016). CEL-Seq2: sensitive highly-multiplexed single-cell RNA-Seq. Genome Biol. *17*, 77.
54. Wangsanuwat, C., Heom, K.A., Liu, E., O'Malley, M.A., and Dey, S.S. (2020). Efficient and cost-effective bacterial mRNA sequencing from low input samples through ribosomal RNA depletion. BMC Genomics *21*, 717.
55. Ashburner, M., Ball, C.A., Blake, J.A., Botstein, D., Butler, H., Cherry, J.M., Davis, A.P., Dolinski, K., Dwight, S.S., Eppig, J.T., et al. (2000). Gene ontology: tool for the unification of biology. The Gene Ontology Consortium. Nat. Genet. *25*, 25–29.
56. Mi, H., Muruganujan, A., Ebert, D., Huang, X., and Thomas, P.D. (2019). PANTHER version 14: more genomes, a new Panther GO-slim and improvements in enrichment analysis tools. Nucleic Acids Res. *47*, D419–D426.
57. Gene Ontology Consortium (2021). The Gene Ontology resource: enriching a gold mine. Nucleic Acids Res. *49*, D325–D334.

STAR★METHODS

KEY RESOURCES TABLE

REAGENT or RESOURCE	SOURCE	IDENTIFIER
Antibodies		
Rabbit polyclonal anti-EIF2α	Cell Signaling	Cat#9722S; RRID:AB_2230924
Rabbit polyclonal anti-p-EIF2α	Cell Signaling	Cat#9721S; RRID:AB_330951
Rabbit polyclonal anti-PKR	Cell Signaling	Cat#3072S; RRID:AB_2277600
Rabbit monoclonal anti-p-PKR	Abcam	Cat#AB32036; RRID:AB_777310
Mouse monoclonal anti-Puromycin	Millipore-Sigma	Cat#MABE343; RRID:AB_2566826
Goat polyclonal anti-rabbit HRP linked IgG	Cell Signaling	Cat#7074P2; RRID:AB_2099233
Goat polyclonal anti-rabbit 680RD IgG	Li-Cor	Cat#926-68071; RRID:AB_10956166
Goat polyclonal anti-mouse 800CW IgG	Li-Cor	Cat#926-32210; RRID:AB_621842
Rabbit monoclonal anti-ATF4	Cell Signaling	Cat#11815S; RRID:AB_2616025
Mouse monoclonal anti-CHOP	Cell Signaling	Cat#2895; RRID:AB_2089254
Mouse monoclonal anti-G3BP1	BD biosciences	Cat#611126; RRID:AB_398437
Rabbit monoclonal anti-p-eIF2α	Abcam	Cat#ab32157; RRID:AB_732117
Goat polyclonal anti-rabbit 633 IgG	Invitrogen	Cat#A21070; RRID:AB_2535731
Goat polyclonal anti-mouse 555 IgG	Invitrogen	Cat#A28180; RRID:AB_2536164
Bacterial and virus strains		
One Shot TOP10 Chemically Competent E. Coli	Thermo Fisher Scientific	Cat#C404010
Chemicals, peptides, and recombinant proteins		
Sodium Arsenite	Sigma Aldrich	Cat# S7400
Puromycin	Thermo Fisher Scientific	Cat# A1113803
DAPI	Thermo Fisher Scientific	Cat# D1306
Fibronectin	Sigma Aldrich	Cat# F1141
DMEM, high glucose	Thermo Fisher Scientific	Cat# 11965
Fetal bovine serum	Atlas Biologicals	Cat#F-0500-D
16% paraformaldehyde	Thermo Fisher Scientific	Cat#28908
1-step transfer buffer	Thermo Fisher Scientific	Cat#84731
TRIzol	Thermo Fisher Scientific	Cat# 15596026
CloneAmp HiFi PCR Premix	Takara	Cat#639298
Gibson Master Mix	New England Biolabs Inc.	Cat#E2611
Critical commercial assays		
Zymo miniprep	Zymo Research	Cat#D4036
Zymo gel extraction	Zymo Research	Cat#D4001
Deposited data		
RNA-seq raw data	This paper	GEO: GSE210019
ISR model	This paper	Attached as supplementary file
Experimental models: Cell lines		
H4	Laboratory of Martin Kampmann	N/A
U2OS	ATCC	ATCC HTB-96
HEK-293T	Laboratory of Jared Toettcher	N/A
Oligonucleotides		
Primers for constructs, see Table S1	This paper	N/A
Software and algorithms		
Python version 3.9.7	Python Software Foundation	https://www.python.org
MATLAB ver. R2020b Update 5	Mathworks, Inc.	https://www.mathworks.com/products/matlab.html

(*Continued on next page*)

Continued

REAGENT or RESOURCE	SOURCE	IDENTIFIER
ImageJ	Schneider et al.[52]	https://imagej.nih.gov/ij/
Nikon NIS-Elements Software	Nikon Instruments Inc.	https://www.microscope.healthcare.nikon.com/products/software/nis-elements
Arduino IDE 1.8.15	Arduino	https://www.arduino.cc/en/software
Other		
96 Well glass bottom plate with high performance #1.5 cover glass	Cellvis	Cat#P96-1.5H-N

RESOURCE AVAILABILITY

Lead Contact

Further information and requests for resources and reagents should be directed to and will be fulfilled by the lead contact, Maxwell Z Wilson (mzw@ucsb.edu).

Materials availability

Requests for reagents will be fulfilled by contacting the lead contact upon reasonable request.

Data and code availability

- Transcriptomic sequencing data have been deposited at Gene Expression Omnibus listed in key resources table. Raw image data reported in this study will be available at reasonable request.
- All data reported in this paper will be shared by the lead contact upon request.
- All original code is publicly available as a supplementary file (Method S1)
- Any additional information required to reanalyze the data reported in this paper is available from the lead contact upon request.

EXPERIMENTAL MODEL AND STUDY PARTICIPANT DETAILS

Cell culture

Human osteosarcoma epithelial cells (U2OS), H4 neuroglioma cells (H4) and HEK293T cells were cultured in Dulbecco's Modified Eagle Medium (DMEM) containing 4.5 g/mL glucose (Gibco), 10% fetal bovine serum (Atlas Biologicals, F-0500-D), 1% penicillin and streptomycin at 37°C and 5% carbon dioxide. All cells carrying light responsive proteins were maintained and treated in the absence of blue light (dark or red light only). Cell culture vessels containing light responsive cells were wrapped in aluminum foil to prevent accidental light leakage. Prior to microscopy experiments, cells were plated onto glass bottom dishes pre-treated with bovine fibronectin to allow for adhesion. All experiments, including drug treatments, were done under dark or red light conditions unless 450nm light illumination was explicitly stated.

METHOD DETAILS

DNA constructs

Plasmids were obtained from Maxwell Z. Wilson and Diego Acosta-Alvear. The DNA regions of interest were amplified from host plasmids by PCR using CloneAmp HiFi PCR Premix (Takara, 639298) with custom primers for Gibson assembly (Table S1). Constructs of interest were generated through subcloning into a lentiviral expression vector bearing the SFFV promoter using Gibson Assembly as per the manufacturer's recommendations. The resulting lentiviral expression vectors contained the chimeric PKR constructs.

Lentivirus transduction

Lentiviral supernatant was produced by transfecting second generation helper constructs, pCMVdR8.91 and pMD2.G (gift of Jared Toettcher, Princeton University), together with our lentiviral constructs at a mass ratio of 0.444 : 0.056 : 0.500, respectively, into HEK-293T cells. Transfections were carried out using polyethyleneimine. HEK-293T cells were maintained for 48 hours post transfection at which point the supernatant was harvested, filtered through 0.45 μm filter and stored at -80 prior to infection of target cells.

Fluorescence activated cell sorting

Engineered cells were sorted using Sony SH-800 cell sorter system. Gating was determined using untransduced parental cells as a negative control, and selected cells were sorted through a narrow fluorescence gate to obtain a pseudo-clonal cell line. All engineered cell lines used in this study originated from expansion of pseudo-clonal cell lines.

Western blotting

Roughly 1 x 10^6 cells per experimental condition were harvested using 1x Laemmli buffer (30 mM Tris-HCl pH 6.8, 1%SDS, 10% (w/v) Glycerol, bromophenol blue) from a single well of a 6-well plate immediately after treatment. The lysates were heated at 95°C for 3 minutes, briefly sonicated, supplemented with 5% 2-mercaptoethanol, and stored at -20°C conditions until SDS-PAGE. Samples were separated in 4%/10% two layer SDS-PAGE gels run at 100V for 1-2 hours, transferred onto PVDF membranes using a TE 77 semi-dry transfer unit (Cytiva Amersham) at 10V for 15 min. The membranes were blocked with 3% BSA in TBS-T for 1 hour, followed by an overnight incubation with primary antibody at 4°C (blots have been cut for different primary stainings). Membranes were washed and incubated with fluorescently or HRP conjugated secondary antibodies for 1 hour at room temperature. All antibodies were diluted in 3% BSA in TBS-T. All incubation steps were followed by 3x washes with TBS-T for 10 min. The membranes were imaged using enhanced chemiluminescence using a Radiance Plus imager (Azure Biosystems) or a Li-Cor Odyssey instrument. Captured blot images were then quantified through ImageJ Fiji macro (ImageJ[52]). All bands were identified and measured in terms of pixel value, whilst subtracting blot background. For phospho/total ratio calculation, we divided phospho lane of appropriate time by total lane. Any calculation done in this manner was taken from same transfer blot, prior to being cut for primary staining.

List of antibodies used in western blotting:

Name	Company	Cat. Number	Species	[c]
eIF2α	Cell Signaling Technology	9722S	Rabbit	1:1000
P-eIF2α	Cell Signaling Technology	9721S	Rabbit	1:1000
PKR	Cell Signaling Technology	3072S	Rabbit	1:1000
P-PKR	Abcam	AB32036	Rabbit	1:1000
Puromycin	Millipore-Sigma	MABE343	Mouse	1:10000
Anti-rabbit HRP linked IgG	Cell Signaling Technology	7074P2	Goat	1:5000
Anti-rabbit 680RD IgG	Li-Cor	926-68071	Goat	1:10000
Anti-mouse 800CW IgG	Li-Cor	926-32210	Goat	1:10000

Puromycilation of nascent peptides

Cells were grown in culture medium until 80% confluency in 6-well plate for a day (one well per condition). Cells were then treated with activating blue light illumination accordingly until 30 min prior to the end of their treatment, at which point, the culture media was replaced with media containing 18 μM puromycin (Gibco, A1113803) and the cells were incubated for an additional 30 min under illumination before sample collection and analysis as described in the Western blotting section.

Immunofluorescence

Cells were grown on fibronectin (Sigma, F1141) coated glass bottom 96 well plates (Cellvis, P96-1.5H-N), washed with PBS, and fixed using 4% paraformaldehyde (PFA, Fisher Scientific, AA433689L) in PBS for 10 minutes at room temperature under dark conditions. Fixed cells were washed with PBS and permeabilized with blocking buffer (0.05% saponin, 0.5% BSA, 50 mM, NH_4Cl in PBS) for 30 min at room temperature. The fixed cells were incubated with primary antibodies diluted in blocking buffer overnight at 4°C. The next day, the cells were washed gently 3x with PBS-T, followed by secondary antibody incubation for 1 hour at room temperature in dark conditions, followed by another round of 3x PBS-T washes. The prepared fixed cells were imaged as detailed in Microscopy imaging.

List of antibodies used in immunofluorescence analyses:

Name	Company	Cat. Number	Species	[c]
ATF4	Cell Signaling Technology	11815S	Rabbit	1:400
CHOP	Cell Signaling Technology	2895	Mouse	1:400
G3BP1	BD biosciences	611126	Mouse	1:400
p-eIF2α	Abcam	ab32157	Rabbit	1:200
Anti-rabbit 633 IgG	Invitrogen	A21070	Goat	1:800
Anti-mouse 555 IgG	Invitrogen	A28180	Goat	1:800

Microscopy imaging

All microscopy imaging, live or fixed, was done using a W2 SoRa spinning-disk confocal microscope equipped with an electron-multiplying charge-coupled device camera (Andor, DU-888) and an incubation chamber maintaining cells at 37°C and 5% CO2.

All cells that were imaged were plated on fibronectin (Sigma, F1141) coated glass bottom 96 well plates (Cellvis, P96-1.5H-N). Images were captured using a 40x NA 1.25 water immersion objective and a 60x NA 1.2 water immersion objective.

Optogenetic stimulation

Engineered photo-switchable proteins were activated using 450 nm blue light. For Western blot experiments with maximal light activation of the pathway, we utilized a custom 36 LED plate mounted on a box lined with aluminum foil, allowing for equal light distribution throughout the box. For confocal imaging, 450 nm light was delivered through laser at 100% power using a 40x NA 1.25 water immersion objective. For spatial patterning of light, we utilized purpose-built microscope-mounted LED-coupled digital micromirror devices (DMDs) triggered via Nikon NIS Elements software, allowing us to specify the exact parameters of light delivery at each coordinate of our imaging plane. For precisely modulated IF experiments, we utilized the benchtop LED array light delivery device (optoPlate), per authors instructions.[14] The light delivery parameters for the optoPlate were purpose-set for each experiment, where stimulating light was continuously ON or OFF, without pulsing, and 4 to 121 $\mu W/cm^2$, as measured by THORLabs power meter, range of intensities applied translates as 3-96 on the intensity setting of the optoPlate software. The light illumination sequence of each well included an OFF (dark) period at the start, so that all well illuminations would end at the same time.

Image analysis

All quantification of images followed the same general flow from creating a TIFF library of images to clean-up and analysis using custom code on MATLAB (Figure 3C). Nikon-generated ND2 files were channel separated and converted to TIFF files using ImageJ FIJI macro (ImageJ[52]). The TIFF library of images was organized into separate stacks based on applied treatment (i.e. different intensity of activation, etc.) over time on MATLAB, for ease of access and indexing. All images were then cleaned up to reduce noise through background subtraction and deletion of super bright pixels. DAPI stained nuclei were segmented to identify nuclei as follows: First, we Gaussian-blurred the images, then used threshold detection to identify edges, and watershed transformed the nuclear mask in case of connected nuclei. The nuclear masks were quality checked and the threshold was adjusted manually in case of low quality masking. For nuclear localized information, we applied the nuclear mask to the channel of interest and collected information of every nucleus separately. For cytoplasmic information, we dilated the nuclear mask and removed the mask itself from the dilated mask to quantify the ring around the nucleus as cytoplasmic information. For condensate information, we identified clusters through ''Laplacian of Gaussian'', ''Sobel'' edge detection and intensity-based threshold detection and combined the information to create a condensate mask. We also removed non-condensate information from our mask as follows: outside our size threshold and nuclear localized. Mean intensity, location and area of all objects were saved for quantitative analysis on a single cell level for nuclear and cytoplasmic fluorescence normalized to no treatment control. Condensate data was quantified by summing total condensate intensity across an imaging field and normalized to the number of nuclei detected within said image field to obtain the mean condensate fluorescence per cell. The error bars for condensate data were generated through examining variance of experimental replicates rather than on a cell-to-cell basis.

Bulk RNAseq

Sample treatment and extraction

H4 cells carrying Cry2Olig-PKR cells were plated on fibronectin treated 96-well glass-bottom plate. Cells were illuminated according to experimental set-up using the optoPlate device set to continuous illumination intensity of 121 $\mu W/cm^2$ as mentioned in Optogenetic stimulation. Cells were immediately lysed using 120 μL Trizol (Gibco, 15596026) per well, under red light, and incubation for lysis for 5 min at room temperature. RNA was extracted according to the manufacturer's protocol.

Illumina library preparations

Bulk RNAseq Illumina libraries were prepared following an adaptation of the single-cell method ''CEL-Seq2'' where we treated every illumination duration as a single cell.[53,54] Briefly, sample RNA was reverse transcribed with Cel-Seq2 primer #4 (25 ng) using Superscript II reverse transcriptase. Second Strand Synthesis (SSS) was carried out via *E. coli* ligase (Invitrogen, Cat. # 18052–019) and DNA polymerase I (Invitrogen, Cat. # 18010–025) in SS buffer for 2 hours at 16°C. Next, cDNA was purified with 1:1 AMPure XP DNA beads (Beckman Coulter, Cat. # A63881), and washed with 80% ethanol twice, before elution into nuclease-free water and vacufuge concentrated. *In vitro* transcription was then carried out using MEGAscript T7 kit (Thermo Fisher Scientific, AMB13345) for 13 hours at 37°C, followed by RNA treatment using EXO-SAP (Thermo Fisher Scientific, 78200.200.UL) for 15 min at 37°C, and finally the samples were fragmented (200 mM Tris-acetate (pH 8.1), 500 mM KOAc, 150 mM MgOAc) at 94°C for 3 min before being quenched by 0.5 M EDTA. The fragmented RNA was size selected with 0.8x AMPure RNA beads (RNAClean XP Kit, Beckman Coulter, Cat. # A63987) and eluted in nuclease-free water.

Transcriptome dynamics analysis

Paired-end sequencing of the libraries was performed on an Illumina NextSeq 500, and hits were quantified and z-score normalized per gene. Transcriptomic data was then analyzed through custom pipeline on python packages ''numpy'' and ''pandas''. As data preparation, all genes that were missing entry at any time were removed from data matrix. We then applied SVD function from ''numpy'' to the transcriptome matrix, where rows were distinct genes and columns were duration of stimulation in increasing order. For analysis of dynamics genes were sorted and then plotted based on their rank in their U vector magnitude from SVD of transcriptome matrix. We also applied centroid clustering on the transcriptome matrix through clustermap function of ''seaborn'' package.

Simulating the mathematical model of ISR

Model simulations were conducted in Python 3 using the Anaconda 4.1.3 using the packages ''numpy'', ''pandas'' and ''seaborn''. Numerical simulations were conducted using the ''odeint'' function from the SciPy v1.8.0 scipy.integrate module. All computational experiments can be found in Supplementary Data and Code files (Method S1).

Model derivation was done by using the law of mass action for describing direct interactions and using non-linear hill functions when abstracting multiple protein interaction events. For example, the p-eif2α induced creation of GADD34 involves transcription and translation. Instead of writing down equations that account for the many molecules involved in this process, we opted to represent this process with a hill function, which was constrained to dynamic data. Our reasoning in performing such abstractions was that by limiting the number of free parameters and state variables our model could still be interpretable, enabling us to use it to gain intuition about the ISR.

The ISR model was defined as ISR_coop functions with all the state variables and parameters listed in Figures S4A–S4D, for linear and cooperative models, respectively. Fits to experimental data are detailed in supplementary code files 1 and 2. We defined a time dependent light modulation function, Ustep(t), with a range of [0] to [1] as a proxy for illumination at specific intensities. PKR and p-PKR defined in our model refers to our engineered opto-PKR and its phosphorylated form, and Ustep(t) was incorporated into these state variables. Initial conditions of the state variables were set to 0 for phosphorylated proteins (p-PKR, p-eIF2α) and GADD34, while non-phosphorylated proteins (PKR, eIF2α) were set to 1, as shown at time zero of simulated step response (Figure 4D). All state variables were then plotted using matplotlib plotting library and/or seaborn.heatmap library.

For step response simulation, we set Ustep to [1] at time 2 hrs (of modeled time), and let the simulation run through 20 hours. For intensity scan simulation, we queried the magnitude of Ustep from [0.03] to [1], by increasing it from [0] at 2 hrs of modeled time. For the input-recovery ratio simulation, we pulsed Ustep to [1] starting at 2 hours for corresponding length of modeled time (1.5, 3, or 6) hrs, before pulsing for 30 min (0.5 hrs) at time 10 hours. For simulated stress memory landscape, we log sampled light durations (Ustep == 1) and recovery durations (Ustep == 0), from [0.5] to [10] hours and [2] to [48] hours, respectively, through nested for loop solving the ISR model with odeint for each condition.

Gene ontology analysis

Genes were obtained based on their magnitude in the U vector from our SVD analysis. The top 500 and bottom 500 genes for the first two singular values and were analyzed for over/under representation in biological processes of Homo Sapiens using GO Enrichment Analysis tool (Panther, ''geneontology.org'').[55–57] The dataset used for this analysis was GO biological processes complete set and performed Fisher's exact test with correction for false discovery rate. All biological processes found significant were collapsed onto their parent families.